



The Formation of Microcracks in Water-Saturated Porous Ceramics During Freeze–Thaw Cycles Followed by Acoustic Emission

Tomáš Húlan¹ · Michal Knappek^{2,3} · Štefan Csáki⁴ · Jakub Kušnír^{2,5} · Jana Šmilauerová² · Patrik Dobroň^{2,3} · František Chmelík² · Tiit Kaljuvee⁶ · Mai Uibu⁶

Received: 14 December 2019 / Accepted: 28 December 2020 / Published online: 7 January 2021
© The Author(s), under exclusive licence to Springer Science+Business Media, LLC part of Springer Nature 2021

Abstract

The acoustic emission (AE) technique was employed to monitor crack formation in the water-saturated ceramic material subjected to freeze–thaw cycles. The samples with water accessible porosity ranging from 6 to 50 vol% were prepared from the illite-rich clay by the sacrificing template method. The experimental samples were fired to 1100 °C in the static air atmosphere. Afterward, they were saturated with distilled water and subjected to the freeze–thaw cycles in the temperature range from –22 to 20 °C. The AE signals occurred repeatedly during freeze–thaw cycling and they were attributed to the formation of microcracks in the ceramic body. The intensity of microcracking increased with increasing porosity. The microcracks were created primarily during the freezing stages of the experiment. Nevertheless, a considerable number of microcracks also appeared during thawing, especially in the ceramic body with pores below 1 μm. The microcracking during thawing was attributed to the reabsorption of water by tiny pores.

Keywords Acoustic emission · Illite · Porosity · Ceramics · Frost damage

1 Introduction

Building ceramics exposed to the external environment must meet certain requirements regarding their ability to withstand various effects originating in changing weather conditions. Frost resistance is of paramount importance in regions where the temperature frequently drops below the freezing point of water. Technical standards are available to test the

frost resistance of building materials [1, 2]. These methods are based on subjecting the water-saturated test samples to several freeze–thaw cycles (up to 300) and subsequent visual inspection for the presence of cracks, pop-outs, and/or observation of changes in the relative dynamic modulus of elasticity. These methods rely solely on the *post-mortem* observations after freeze–thaw cycling. Therefore, it is not possible to determine the exact conditions (time and temperature) when the defects are formed.

The frost resistance of a material is affected mainly by its tensile strength, pore size, pore shape, and pore size distribution [3, 4]. It is often stated that materials with smaller pores are more prone to damage than the ones with larger pores [4]. It was found in [4] that frost resistance is inversely proportional to the pore volume and directly proportional to the percentage of pores bigger than 3 μm. Thus, for example, porous bricks can exhibit increased frost resistance if there are enough pores with a diameter above 3 μm. A brick body can expand irreversibly during freeze–thaw loading by 0.2–0.8% [5]. The coefficient of linear thermal expansion (CLTE) of ice has a value of around $50 \times 10^{-6} \text{ °C}^{-1}$, which is considerably higher than CLTE of illite-based ceramic body fired at 1100 °C ($1.15 \times 10^{-6} \text{ °C}^{-1}$). The pressure of

✉ Tomáš Húlan
thulan@ukf.sk

¹ Constantine the Philosopher University, Tr. A. Hlinku 1, 94974 Nitra, Slovakia

² Charles University, Ke Karlovu 5, 12116 Prague, Czech Republic

³ Nuclear Physics Institute of Czech Academy of Sciences, Řež 130, 250 68 Řež, Czech Republic

⁴ Institute of Plasma Physics of The Czech Academy of Sciences, Za Slovankou 1782/3, 182 00 Prague, Czech Republic

⁵ Czech Technical University in Prague, Trojanova 13, 120 00 Prague 2, Czech Republic

⁶ Tallinn University of Technology, Ehitajate tee 5, 19086 Tallinn, Estonia

expanding ice is, however, often not the main reason for frost damage [6].

There are several theories regarding the effect of frost on porous materials [6]. Most of them were originally developed for concrete or hardened cement paste, but they can be adopted for traditional ceramics due to the similar character of these materials. The simplest model of frost damage is based on the effect of internal pressure caused by expanding water when it undergoes a liquid–solid transition accompanied by a volume change of ~9% [3, 6, 7]. The theory of frost damage by expanding water proved to be not entirely satisfactory and more sophisticated theories were developed. The hydraulic pressure theory proposed by Powers [8] ascribes the internal pressure to the forced movement of water expelled from the pores by formed ice crystals. The basic principle of this theory, i.e. the expulsion of water from capillary pores, was disputed several years later by Powers and Helmuth [9]. They, as well as other researchers later, found that water is absorbed by the capillary pores, rather than expelled from them [6, 9]. The explanation in terms of thermodynamics states that during freezing, ice is formed in the capillary pores (10^1 – 10^4 nm), while water in even smaller gel pores (0.5–10 nm) becomes undercooled. Since the free energy of ice is lower than the free energy of water, the potential energy forces water towards the capillary pores. This explanation was further extended considering the fact that water in the pores of concrete usually contains dissolved chemical compounds (mostly N_2O and K_2O), increasing the osmotic pressure [10]. Another mechanism of frost impact on porous materials, with similar consequences, was proposed by Litvan [11, 12]. In his model, the forced movement of water towards the sites with formed ice can be explained by counter-balancing the vapor pressure above the ice surface and the surface of supercooled water in the pores. Vapor pressure difference (i.e. the decrease in the relative humidity above the surface of undercooled water in the pores) leads to the desorption of water from the smallest pores. The desorbed water diffuses towards larger pores (or material surface) where it freezes. As the temperature decreases below 0 °C, large pores are desorbed first, and the desorbed water is transported towards the surface of the body, where it freezes. The small pores are then desorbed on further cooling and the water freezes in larger pores. Nevertheless, a unified theory of the impact of frost in porous materials still does not exist because it is next to impossible to take into account all the possible variables [6].

The models of frost action can explain the forces that cause the structural deterioration and, in some cases, also the specific circumstances at which these forces are maximal (temperature, saturation level, porosity, etc.). To confirm the predictions of these theories, however, one needs a tool that is capable of determining in-situ the exact stages of crack formation. The acoustic emission (AE) technique can be a

convenient method for this task [13]. Furthermore, AE is capable of detecting microcracks which might not be observable by a visual inspection.

AE signals are elastic waves originating from localized microstructural changes in the material. These waves are transformed into an electrical signal via a piezoelectric transducer, digitalized by an analog-to-digital converter and stored in a computer. In ceramic materials, elastic waves are generated mainly during the formation of microcracks [13, 14]. AE was previously employed to study the freeze–thaw behavior of concrete and mortars [15–19]. In [15], it was found that in mortar saturated with NaCl solution, most of the AE events occurred slightly after the temperature of the sample reached the liquidus line on cooling. AE was also used to identify the temperature at which the frost damage begins to occur in concrete pavement joints during cooling (–8 °C) [16]. The application of AE during the freezing of water in concrete was reported in [17]. The highest AE activity was observed during the first three freeze–thaw cycles. The AE signals were observed mainly in the thawing stages of the experiment, however, no particular explanation was proposed by the authors. In the same study, the impact echo method revealed a shift in the natural frequency of vibration after six freeze–thaw cycles as a consequence of microstructural changes. In [18, 19], AE was used to study the microcracking in concrete saturated with NaCl solution in various concentrations. Cyclic tests (up to 3 cycles) revealed a decreasing amplitude of AE events with an increasing number of cycles. As in [17], the AE activity was observed during thawing, but no explanation was given in neither of these studies. In our recent study [20], the deterioration of mechanical properties of the illite-based ceramics with varying porosity was assessed via the changes in the resonant frequency of free flexural vibrations and internal damping. It was concluded that the samples with higher porosity exhibited lower frost resistance. However, no further deterioration of the mechanical properties was observed if the porosity exceeded 42%.

Previous studies that employed AE to monitor cracks formation during freeze–thaw experiments, as mentioned above, were focused primarily on concrete or mortar. These materials differ from ceramic materials mainly by their mineralogical and chemical composition, but also by interparticle bonding and possible frost damage mechanisms. For example, an interaction between aggregates and cement paste when concrete freezes can influence the frost resistance of the material [6]. Even though the building ceramics (i.e. bricks, roof tiles, floor tiles, wall tiles, etc.) are often exposed to external environments causing frost damage, there are no data available in the literature regarding in-situ AE measurements during water freezing in these ceramic materials. The main goal of this research was to attempt such experiments and explore their viability. Moreover, the

dependence of AE activity on porosity was also studied, as there is a complete lack of such works. To this end, the AE technique was applied to monitor water-saturated illite-based ceramics with varying porosity subjected to freeze–thaw conditions. This material was chosen as a model material because it can represent a large group of materials belonging to building ceramics.

2 Materials and Methods

The methodology of sample preparation followed our previous research [20]. In short, the experimental samples were prepared from the illite-rich clay (IRC) and charcoal serving as a template for developing the porosity. IRC, which was mined in the Tokaj region in north-eastern Hungary, was milled and sieved to obtain a powder with particles below 100 μm . The mineralogical composition of IRC was as follows [21]: 80 wt% illite, 12 wt% quartz, and 8 wt% feldspar. A clay rich in illite was chosen because illite is, besides kaolin, a clay mineral most frequently found in raw materials used for the production of traditional ceramics [22–24]. Commercially available charcoal was crushed in a mortar and sieved until the whole batch passed a 100 μm sieve. According to the thermogravimetry and differential thermal analyses (unpublished results), thermal oxidation (i.e. burning) of charcoal in the air atmosphere takes place in the temperature interval of (300–520) $^{\circ}\text{C}$. During the firing of ceramic bodies containing charcoal, void spaces (pores) are formed at the original locations of charcoal grains.

Four experimental mixtures, containing 5 (denoted as IC5), 10 (IC10), 20 (IC20), or 30 (IC30) wt% of charcoal, were prepared according to Table 1. After mixing of the materials in a dry state, deionized water was added into the mixtures. The amount of water in the obtained slurry was about 56 wt%. The slurry was afterward poured into gypsum molds and left to dry freely. The dried samples were cut and ground to the final dimensions of $10.5 \times 8.7 \times 20 \text{ mm}^3$. Finally, holes of 3 mm in diameter and 5 mm deep were drilled into the center of one of the $8.7 \times 20 \text{ mm}^2$ faces of each sample. Before the freeze–thaw (F–T) experiments, the samples were fired in an electric furnace to the maximum temperature of 1100 $^{\circ}\text{C}$ at the heating rate of 5 $^{\circ}\text{C}\cdot\text{min}^{-1}$ and cooled freely. An alumina rod, which served as a waveguide for the AE measurements, was firmly mounted into

the holes, following the approach applied in our previous paper [25]. After firing, the samples for F–T experiments were fully saturated with water by boiling in deionized water for 2 h. Then, the samples were wrapped in a plastic foil to prevent drying during the experiments. Small pieces of material ($\sim 0.45 \text{ g}$) for mercury intrusion porosimetry were obtained by crushing one of the samples from each mixture after the firing.

The morphology of raw powders and the microstructure of fired samples were analyzed using the scanning electron microscope (SEM) FEI Quanta FX200 operating in the backscattered electron detection mode. The fired samples were mechanically polished with a final step of 3 μm diamond paste and cleaned in ethanol in an ultrasonic bath. The particle size distribution of the input materials was obtained by the laser beam scattering method using the instrument Horiba LA-950. The mercury intrusion porosimetry was used to determine the pore size distribution of fired samples using the Quantachrome PoreMaster GT apparatus. Bulk density ρ_b and water-accessible porosity P_a were determined by the boiling method according to ASTM C 373–88. Matrix density ρ_m was measured using the helium pycnometer Pycnomatic ATC-Multi. He-accessible open porosity P_t was calculated from the bulk density and the matrix density as $P_t = [1 - (\rho_b/\rho_m)]$.

The temperature program for one F–T cycle was as follows: cooling from 20 to $-22 \text{ }^{\circ}\text{C}$ at the rate of $-2 \text{ }^{\circ}\text{C}\cdot\text{min}^{-1}$; 50 min isotherm; heating to 20 $^{\circ}\text{C}$ at the rate of 3 $^{\circ}\text{C}\cdot\text{min}^{-1}$; 30 min isotherm. Each sample was subjected to 310 F–T cycles. Note, that the temperature controller monitored the temperature of the surrounding air in the close vicinity of the sample, not the sample itself. For this purpose, another thermocouple was fixed on the surface of the sample.

Differential scanning calorimetry (DSC) was performed using the Mettler Toledo DSC 822e device. Small pieces of each sample for DSC were saturated with water and after removing the excess water from the surface they were weighted ($\sim 10 \text{ mg}$) and placed into aluminum DSC crucibles covered with an aluminum lid. The temperature program for the DSC experiments was identical to the program used for the F–T experiments (see above).

The AE signals were collected during thermal cycling by the piezoelectric transducer MST8S ($\text{Ø}3 \text{ mm}$, a flat response in a frequency band from 100 to 600 kHz, sensitivity 55 dB) coupled with the Dakel preamplifier (gain of 35 dB) and processed using the DAKEL-XEDO-3 AE system. The experimental setup is depicted in Fig. 1. The transducer was glued on top of a 10 cm long $\text{Ø}3 \text{ mm}$ alumina (sintered Al_2O_3) rod. The opposite side of the alumina rod was mounted into the predrilled hole in the sample (as mentioned above). Both the hole and the end of the alumina rod had a conical shape to ensure good contact. The water-saturated samples with mounted waveguide and AE transducer were placed into an in-house developed

Table 1 The composition of experimental samples

	Mixture code			
	IC5	IC10	IC20	IC30
Illite-rich clay [wt%]	95	90	80	70
Charcoal [wt%]	5	10	20	30

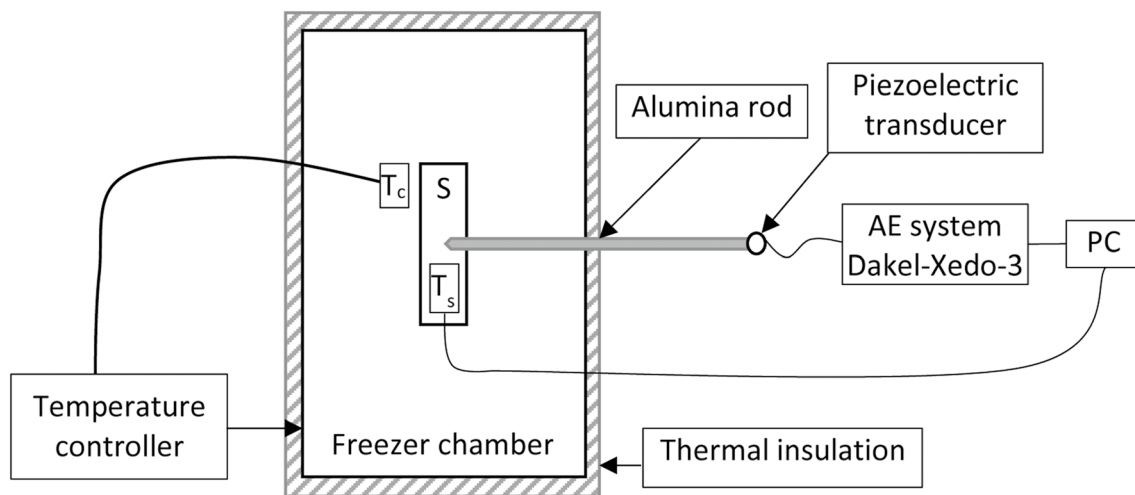


Fig. 1 The scheme of the experimental setup: *S* sample; T_c temperature sensor of the chamber; T_s temperature sensor at the sample's surface; *PC* computer

Peltier element freezer cell with temperature control capability. The AE signals were evaluated by means of the so-called *AE count rate* [s^{-1}], i.e. the number of times the AE signal exceeds a predefined threshold value (set slightly above the noise level) in a time window of 1 s, and *AE event amplitudes* [mV]. The threshold for the AE count rate as well as for the AE event detection was set to 149 mV (11.5 dB). The fullscale of A/D converter was ± 1000 mV. The sampling rate was 4 MHz. For AE event individualization, the hit definition time (i.e. the “dead time”) of 1007 μs was used—each AE event was ended if the signal remained below the threshold level for 1007 μs . Note that the hit lockout time—the second individualization parameter used in some AE systems—is not implemented in the Dakel Daemon control software, i.e. the new AE event could be recorded immediately after the previous one ended. No artificial AE signals were recorded during the preliminary experiments on water-saturated samples, using an identical experimental setup. This assertion was also confirmed by the absence of AE signals during the test measurements on dry samples. For this reason, conventional threshold-based detection was sufficient enough to separate real signals from the background noise. The AE counts and events were collected during cycle intervals of 1–10, 51–60, 101–110, 201–210, and 301–310 for each sample, which provided representative sets of data sufficient for the analyses performed in this study.

3 Results

3.1 Characterization of Materials

The SEM micrographs of the raw material powders are presented in Fig. 2. The IRC material contained agglomerates of

plate-like crystals of illite [26] and equiaxed quartz grains. Charcoal particles were of an irregular shape and a significant fraction of them were elongated along original wood fibers. The particle size distribution of the used materials is shown in Fig. 3. The IRC particles of the size around 2 μm are typical of ceramic clays [27]. The maximum in the particle size distribution at around 30 μm can be attributed to the agglomerates of illite crystals and grains of quartz. Charcoal exhibited a multimodal distribution of particle sizes with maxima at (10, 90, and 300) μm . The presence of a small fraction of charcoal particles with an equivalent spherical diameter above 100 μm , despite using the 100 μm sieve, can be attributed to the elongated shape of charcoal particles (cf. Fig. 2b).

3.2 Porosimetry

The pore size distribution of the samples after firing at 1100 $^{\circ}C$ identified by mercury intrusion porosimetry is presented in Fig. 4 (solid lines). An increasing amount of charcoal led to the formation of bigger pores as can be also seen from a shift of the maximum in the pore size distribution towards larger values (see also SEM micrographs in Fig. 9 before F–T cycling). This can be explained by the agglomeration of charcoal particles, despite thorough mixing.

The bulk density gradually decreased with increasing additions of charcoal before firing from 2.03 to 1.24 g/cm^3 for IC5 and IC30, respectively (Table 2). On the other hand, the matrix density slightly increased which can be explained by a lower fraction of closed pores in the mixtures with higher charcoal content. The He-accessible porosity reached the highest values as compared to the Hg- and water-accessible porosity, because the pores down to 0.2 nm

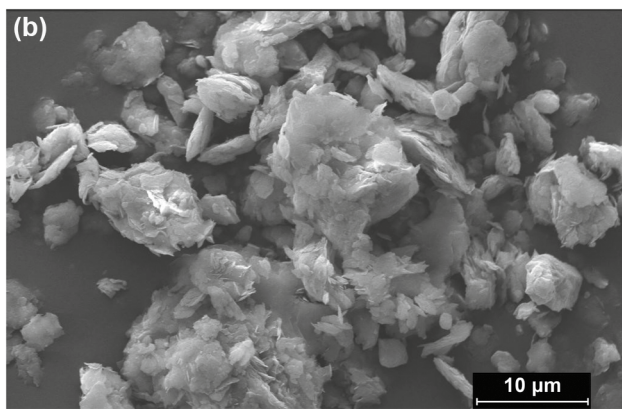
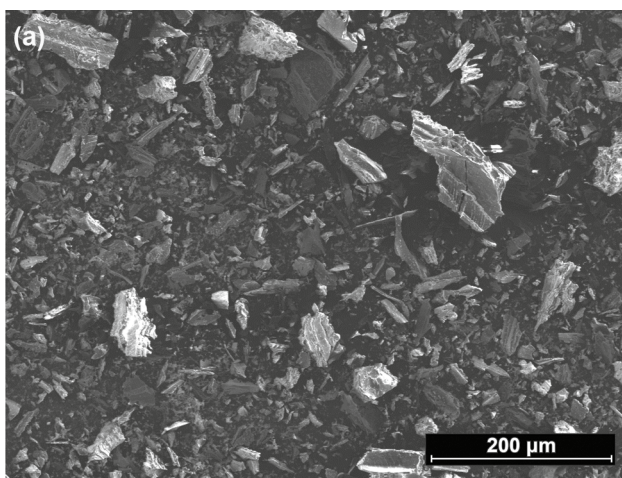


Fig. 2 The SEM micrographs of a the IRC material and b the charcoal particles

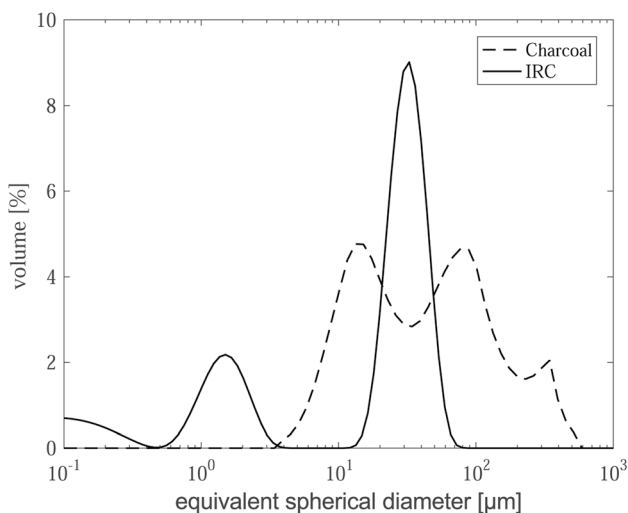


Fig. 3 Particle size distribution of the IRC and charcoal powders

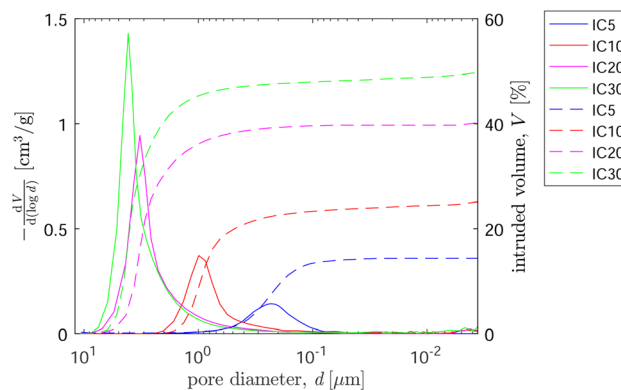


Fig. 4 The pore size distribution of fired samples (solid lines) and the volume (V) of intruded pores normalized to the sample mass (dashed lines)

Table 2 The bulk density, matrix density, and porosity determined by various methods of experimental samples after firing at 1100 °C

	IC5	IC10	IC20	IC30
Bulk density [g/cm ³]	2.03	1.87	1.46	1.24
Matrix density [g/cm ³]	2.36	2.49	2.53	2.53
He-accessible porosity [vol%]	20	30	47	55
Hg-accessible porosity [vol%]	14	25	40	50
Water-accessible porosity [vol%]	5.8	20	40	50

The relative uncertainties were below 1%

can be detected by this method. From the point of view of the frost action on the ceramic body, the most relevant quantity is the volume of pores accessible to water. As can be seen in Table 2, not the entire volume of open pores was accessible to water in the case of samples IC5 and IC10 (i.e. with low initial charcoal content). Considering the pore size distribution (Fig. 4) the minimal diameter of pores accessible to water was ~0.4 μm for IC5 and IC10. The open pores (detectable by Hg-porosimetry, Fig. 4) were fully accessible to water in the case of samples IC20 and IC30 as they virtually did not contain pores below ~0.4 μm.

3.3 Differential Scanning Calorimetry

The heat flow curves of water-saturated samples are shown in Fig. 5. For better visibility, some segments of the measurements were omitted. It is observed that the areas of the heat flow peaks during cooling, which correspond to ice crystallization, were proportional to the initial content of charcoal. From the position of peak onsets, it is clear that absorbed water did not freeze at 0 °C, but became undercooled and froze between -9 and -11 °C. The temperature at which water started to freeze did not correlate with the charcoal content. The reason can be the effect of pore

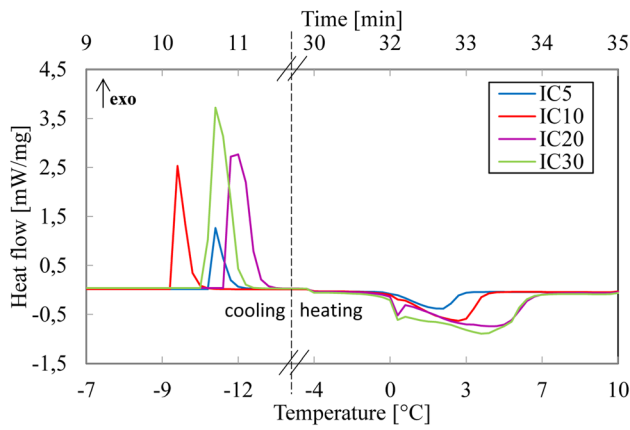


Fig. 5 The heat flow curves of water-saturated samples. Some segments of the measurement were omitted for the sake of better visualization

diameter (smaller pores cause higher undercooling [28]) and the volume of absorbed water (due to limited heat transfer rate in DSC experiments). On heating, the onset of the endothermic peak corresponding to the melting of ice is localized at ~0 °C for all types of samples. The peak itself was

broader in the case of samples with higher porosity and its termination was localized at 3 °C and 4 °C for the samples IC5 and IC10, respectively; and at 6 °C for both the samples IC20 and IC30.

3.4 Acoustic Emission During the Freeze–Thaw Experiments

The recorded AE counts, amplitudes, and temperature measured at the surface of the samples as a function of time are shown in Fig. 6. For each sample, only the first and last ten F–T cycles are shown (i.e. the cycles 1 to 10 and 301 to 310). The dependence of the AE data (in terms of AE count rate and AE event amplitudes reflecting the dynamics of microcracking within the samples) on the temperature was observed and the AE response followed the periodicity of the temperature program rather accurately. Comparing the AE activity (counts) and the AE intensity (amplitudes), it is evident that these quantities correlate quite well even though they capture different aspects of microcracking dynamics. Figure 6 gives evidence that the AE counts were more abundant during the first F–T cycles than during the last F–T cycles for all samples. This is quantified in more detail in

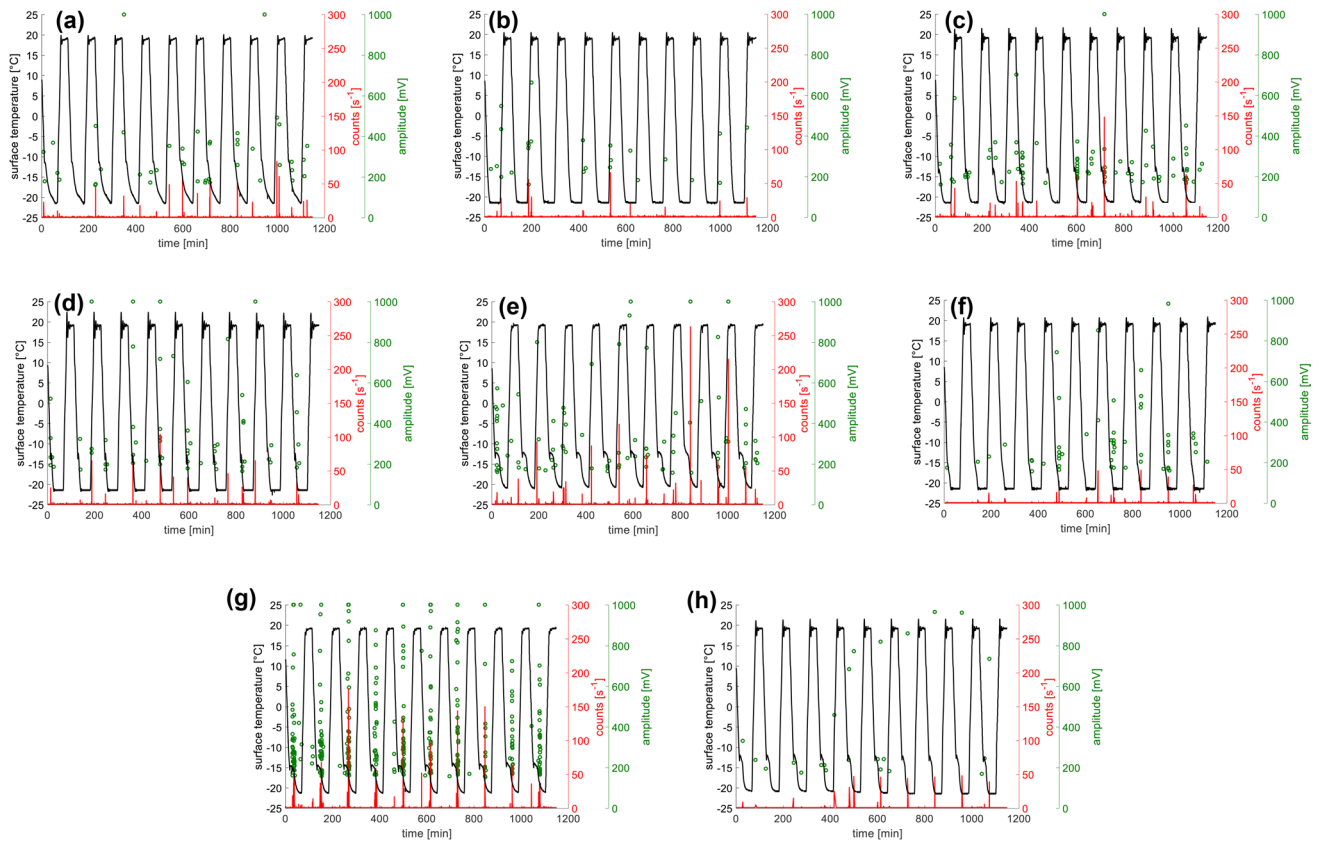


Fig. 6 The AE signals and the recorded surface temperature at sample surface for the samples with different porosity and for various F–T cycles: **a** IC5: 1st–10th cycle; **b** IC5: 301st–310th cycle; **c** IC10:

1st–10th cycle; **d** IC10: 301st–310th cycle; **e** IC20: 1st–10th cycle; **f** IC20: 301st–310th cycle; **g** IC30: 1st–10th cycle; **h** IC30: 301st–310th cycle

Fig. 7a which summarizes the total number of counts during F–T cycles: 1st to 10th, 51st to 60th, 101st to 110th, 201st to 210th, and 301st to 310th. Note that the AE count rate below 5 s^{-1} could originate in the background noise as the threshold level was set only slightly above the noise level and, thus, was omitted from the summation.

Surprisingly, the highest AE activity was not observed during the first F–T cycles. In the case of the samples with high porosity (IC20 and IC30), the maximum of AE activity was observed between the 51st and 60th cycle. Further thermal cycling of these two samples caused much lower AE activity, which dropped to approximately (10–20) % of the highest AE activity. The maximum AE activity of the sample IC10 was recorded during 101st through 110th F–T cycle. No clear trend was observed in the case of IC5 samples with the lowest porosity. It was also generally observed that the total number of AE counts increased with increasing charcoal content in the raw mixtures (i.e. with increasing

porosity). This result confirms the notion that more water in the pores causes more structural damage upon freezing.

Complementary information was also given in terms of the AE event amplitudes which are closely related to the energy of AE events. The AE amplitudes grew with increased sample porosity and, moreover, a greater fraction of large amplitudes ($> 500 \text{ mV}$) seems to be present during the later cycles (301st to 310th) compared to the first ones—especially for the IC10 and IC30 samples, even though there are substantially fewer events. In other words, this observation suggests that the cracking is more energetic when the pores are larger and also during the later stages of cycling, when smaller microcracks are likely already formed in the microstructure.

Besides, in the stacked plot in Fig. 7a, the counts detected during heating and cooling stages are separated. The sample IC5 with the smallest pores exhibited a practically equal number of AE counts (i.e. microcracks) during the heating segments as during the cooling segments. On the contrary, the sample IC30 with the highest porosity exhibited microcracking almost exclusively during the cooling segments. The ratio of the AE activity in the samples IC10 and IC20 during the heating and cooling segments depended on the number of F–T cycles and even though no clear trend was observed as a function of porosity, more AE counts were observed, on average, during freezing. These results suggest that the materials with small pores tend to undergo more intensive microcracking during the thawing than the materials with large pores.

An inverse trend was observed in the evolution of the cumulative AE counts and the Young’s modulus of the samples exposed to the same thermal cycling, Fig. 7b. The rates of increase in the cumulative AE counts (i.e. a proxy of the microcracking activity) and decrease in the Young’s modulus (reflecting overall structural degradation), give at least qualitative evidence for the progressive microcracking-induced damage in all the samples.

For a deeper analysis, the first three F–T cycles of the sample IC20 are shown in Fig. 8. This sample was chosen because it showed high AE activity on heating stages during the first ten F–T cycles (Fig. 7a). The exothermic effect due to water freezing was reflected in the measured surface temperature on cooling. This effect occurred at approximately $-12.3 \text{ }^\circ\text{C}$. This is in good agreement with the DSC measurements of the IC20 sample which showed that the freezing point was shifted down to the temperature of about $-11.5 \text{ }^\circ\text{C}$ (cf. Fig. 5). The thawing, on the other hand, started almost exactly at $0 \text{ }^\circ\text{C}$, as determined also by DSC. The effect of thawing, however, was not significantly reflected in the measured surface temperature, Fig. 8. Despite the correlation of AE events with temperature is rather good, it is not perfect. Most of the AE events occurred at the temperature of around $-12 \text{ }^\circ\text{C}$, i.e. at the

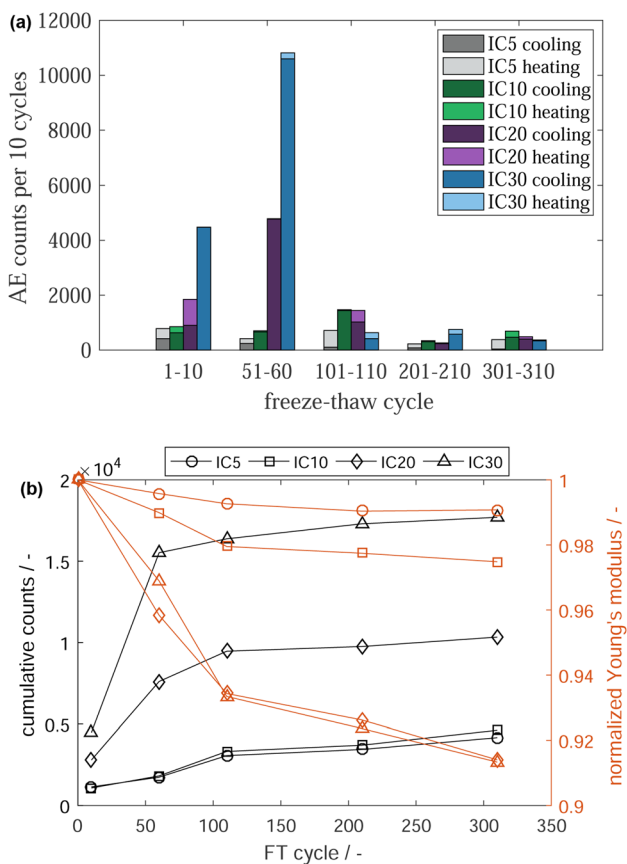


Fig. 7 a The sum of AE counts over 10 freeze–thaw cycles, divided into freezing and thawing segments. Counts below 5 s^{-1} were omitted from the summation due to possible effect of the background noise (the threshold level was set very close to the noise level); b the Young’s modulus normalized to initial values and the cumulative AE counts

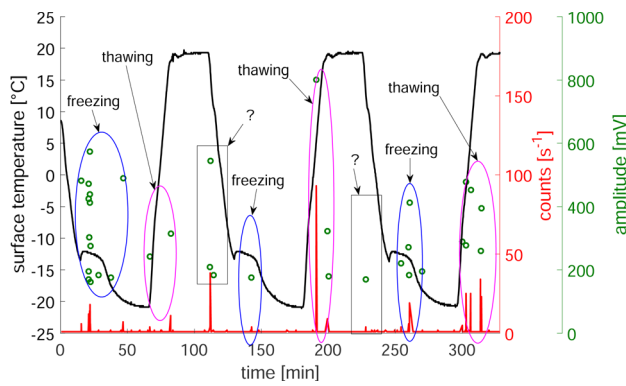


Fig. 8 The AE signals and the recorded surface temperature of the sample IC20 for 1st–3rd F–T cycle

freezing point of water (blue line ellipses in Fig. 8). This holds only for the first and third cooling segment in Fig. 8. Only a weak AE signal was recorded during the second cooling segment. There are some AE events detected on cooling that occurred at higher temperatures well above 0 °C (rectangles in Fig. 8). The origin of these signals is not clear at the moment. We speculate that they can be attributed to relaxation processes related to thermal contraction as the temperature decreases. In the case of this sample, a relatively high number of AE events occurred on heating (magenta ellipses in Fig. 8). These events are not localized in such a narrow temperature interval as in the case of the events occurring during cooling. The AE events during heating were also observed elsewhere [17, 18].

3.5 Microstructure Evolution

In Fig. 9, the SEM images of polished surfaces of the experimental samples are shown, both before and after thermal cycling. The microstructure is characterized by vitrified areas (V), grains of quartz (G), and pores (P). A higher number of voids (pores) is visible in samples with a higher amount of charcoal added before firing. The pores had elongated shapes, similar to original charcoal particles. There are no significant changes observed in the microstructure of ceramic samples before and after the F–T treatment. Neither it is possible to distinguish individual microcracks from the intrinsic porosity. The amount and sizes of the microcracks are probably too small to be observable in the sample's cross-section. This finding supports the suitability of the AE technique for the study of frost damage as it allows *in-situ* detection of microcracks from the entire sample volume, which are otherwise not observed by the standard microscopic techniques providing only local information with limited resolution.

4 Discussion

Considering the simplest model of frost damage caused by expanding ice during its crystallization, it is viable to ascribe the more pronounced microcracking in the samples with greater porosity to the volume of absorbed water. It would be also rational to expect that most of the microcracks were formed during the first freezing cycle. The microcracks, however, appeared also during repeated F–T cycles (Fig. 6). This phenomenon can be explained by considerations emanated from the more advanced Litvan's model [11, 12]. Water leaving capillary pores accumulates in the new microcracks and, during the next freezing cycle, its expansion causes the creation of more microcracks [6]. A successive enlargement of the cracks can provide at least a partial explanation of why the maximum in the AE activity was not observed during the first F–T cycles, but rather during the 51st to 60th cycle (Fig. 7a).

The observation of the AE activity during heating/thawing of water in the pores is rather counter-intuitive. Such an effect was, however, observed also elsewhere [17–19]. The models which are standardly used to explain frost damage (crystallization pressure, hydraulic pressure, osmotic pressure) cannot explain microcracking on heating/thawing. Here we propose an explanation in terms of the Litvan's model [11]: The reabsorption of water to the smallest pores takes place when temperature increases in the water-saturated samples. This can be accompanied by volume changes in the sample, as was shown in [11]. This phenomenon could account for microcracking taking place during the heating segment (especially during thawing) if the volume changes are not uniformly distributed in the sample volume. This also agrees with the observation that the material with small pores (IC5) tends to show a relatively high AE activity on heating. The rate of temperature change can play an important role in this process, which might be an interesting subject of further studies.

The results of the development of the normalized Young's modulus and the cumulative AE counts with the F–T cycles suggest that the deterioration of mechanical properties due to microcracking reaches some sort of saturation. Increased microcracking of IC30 as compared to IC20 (Fig. 7b) did not cause any further decrease in the Young's modulus. A possible explanation can be found in an unequal contribution of the individual microcracks to the deterioration of mechanical properties. For example, in the porous structure of the sample IC30 (Fig. 9g, h) the cracking around larger grains, or cracking in the denser areas can have a higher influence on mechanical properties than the cracking of thin walls or already detached grains (Fig. 9g).

To the author's best knowledge, this study is the first attempt to monitor the microcracking *in-situ* during the

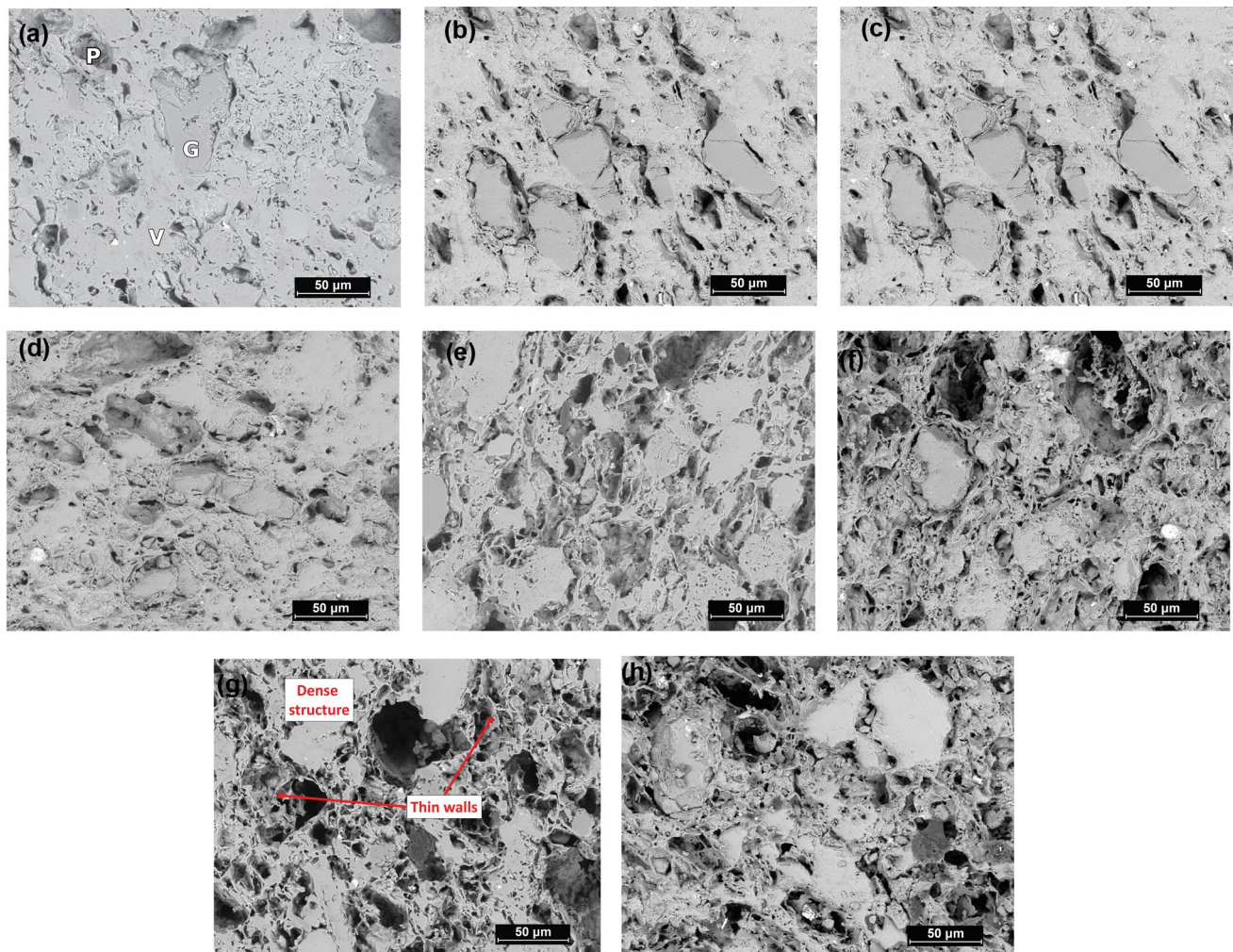


Fig. 9 The SEM microstructure observations of polished surfaces of the experimental samples after 0 and 310 freeze–thaw cycles. **a** IC5: 0 cycles; **b** IC5: 310 cycles; **c** IC10: 0 cycles; **d** IC10: 310 cycles; **e** IC20: 0 cycles; **f** IC20: 310 cycles; **g** IC30: 0 cycles; **h** IC30: 310 cycles

F–T cycling of ceramic material using the AE technique. Moreover, there are only a few studies dedicated to concrete and mortars which applied a similar methodology. Considering the limited amount of available data, it is difficult to thoroughly assess the differences between the dynamics of microcracking in ceramics and concrete or mortar during the F–T conditioning. However, taking into account the available data [17–19] and the results of this study, it seems that the microcracking in ceramics has a more stochastic nature. As visible in Fig. 6, in some of the F–T cycles almost no AE activity was detected while there was high activity in the later F–T cycles (see for example the 5th and the 6th cycle in Fig. 6c). On the other hand, the AE activity seems to decrease quite rapidly with the F–T cycle in cementitious materials [18]. Further studies will be needed to determine the role of an abundance of possible experimental and material variables on the frost damage in ceramic materials.

5 Conclusions

The creation of microcracks during freezing–thawing cycles of water-saturated illitic ceramic samples with controlled porosity was investigated using the *in-situ* monitoring of acoustic emission response. In summary, it was found that:

- the creation of microcracks follows the periodicity of the freeze–thaw cycles, which was attributed to water accumulated in new microcracks during thawing, causing further damage during repeating freezing;
- the microcracking increases with increasing porosity (i.e. with the amount of absorbed water) confirming that more water in the pores causes more structural damage upon freezing;
- the microcracks are created during both freezing and thawing of water in the ceramic body, whereby the microcracking during freezing is more abundant;

- the formation of microcracks is more intense during the thawing of water in the samples with smaller pores. This can be attributed to the reabsorption of water into the smallest pores during thawing, following Litvan's model.

The experiments presented here are believed to be the first attempt to monitor microcracks formation due to ice formation in-situ in the ceramic material. The acoustic emission proved to be an effective tool for this task. The model material used in this work is a representative material for the wide group of building ceramics (bricks, tiles, etc.). The obtained results can, therefore, contribute to the general understanding of frost damage in the ceramic materials. Further research can be focused on the influence of heating/cooling rate, correlation with other material properties such as mechanical strength, mineral composition, etc.

Acknowledgements This work was financially supported by the Czech Science Foundation (Grant No. 17-16772S), by the grant VEGA 1/0810/19 from the Ministry of Education of the Slovak Republic, and by the institutional research funding body (Grant No. IUT33-19) of the Estonian Ministry of Education and Research. M.K. acknowledges financial support from OP RDE, MEYS (Grant No. CZ.02.1.01/0.0/0.0/16 013/0001794).

References

1. ASTM C 666/C 666M-03, ASTM Standard C 666/C 666M-03, ASTM C 666/C 666M-03: Standard Test Method for Resistance of Concrete to Rapid Freezing and Thawing. ASTM International, Philadelphia, USA (2003)
2. Standard Test Method for Measuring the Resistance of Ceramic Tile to Freeze-Thaw Cycling (2002)
3. Ikeda, K., Kim, H.S., Kaizu, K., Higashi, A.: Influence of firing temperature on frost resistance of roofing tiles. *J. Eur. Ceram. Soc.* **24**, 3671–3677 (2004). <https://doi.org/10.1016/j.jeurceramsoc.2003.12.014>
4. Maage, M.: Frost resistance and pore size distribution in bricks. *Matériaux Constr.* **17**, 345–350 (1984)
5. Šveda, M., Sokolář, R.: The effect of firing temperature on the irreversible expansion, water absorption and pore structure of a brick body during freeze–thaw cycles. *Mater. Sci.* **19**, 465–470 (2013). <https://doi.org/10.5755/j01.ms.19.4.2741>
6. Pigeon, M., Pleau, R.: *Modern Concrete Technology 4: Durability of Concrete in Cold Climates*. Taylor & Francis, London (2010)
7. Šveda, M.: Effect of water absorption on frost resistance of clay roofing tiles. *Br. Ceram. Trans.* **102**, 43–45 (2003). <https://doi.org/10.1179/096797803225009210>
8. Powers, T.C.: The air requirement of frost-resistant concrete. *Proc. Highw. Res. Board.* **29**, 184–211 (1949)
9. Powers, T.C., Helmuth, R.A.: Theory of volume changes in hardened Portland cement pastes during freezing. *Proc. Highw. Res. Board.* **32**, 285–297 (1953)
10. Powers, T.C.: *Freezing Effects in Concrete*. American Concrete Institute, Deroit (1975)
11. Litvan, G.G.: Phase transitions of adsorbates. III. Heat effects and dimensional changes in nonequilibrium temperature cycles. *J. Colloid Interface Sci.* **38**, 75–83 (1972). [https://doi.org/10.1016/0021-9797\(72\)90221-4](https://doi.org/10.1016/0021-9797(72)90221-4)
12. Litvan, G.G.: Phase transitions of adsorbates: IV, mechanism of frost action in hardened cement pastes. *J. Am. Ceram. Soc.* **55**, 38–42 (1972). <https://doi.org/10.1080/01411599908224536>
13. Knappek, M., Húlan, T., Minárik, P., Dobroň, P., Štubňa, I., Stráská, J., Chmelík, F.: Study of microcracking in illite-based ceramics during firing. *J. Eur. Ceram. Soc.* **36**, 221–226 (2016). <https://doi.org/10.1016/j.jeurceramsoc.2015.09.004>
14. Húlan, T., Štubňa, I., Kaljuvee, T., Csáki, Š., Knappek, M., Dobroň, P., Chmelík, F.: Acoustic emission of Estonian clay Arumetsa during firing. *AIP Conf. Proc.* **1988** (2018). <https://doi.org/10.1063/1.5047610>
15. Qian, Y., Farnam, Y., Weiss, J.: Using acoustic emission to quantify freeze-thaw damage of mortar saturated with NaCl solutions. *Proc. 4th Int. Conf. Durab. Concr. Struct.* (2014). <https://doi.org/10.5703/1288284315379>
16. Li, W., Pour-Ghaz, M., Castro, J., Weiss, J.: Water absorption and critical degree of saturation relating to freeze–thaw damage in concrete pavement joints. *J. Mater. Civ. Eng.* **24**, 299–307 (2012). [https://doi.org/10.1061/\(ASCE\)MT.1943-5533.0000383](https://doi.org/10.1061/(ASCE)MT.1943-5533.0000383)
17. Pazdera, L., Topolar, L.: Application acoustic emission method during concrete frost resistance. *Russ. J. Nondestruct. Test.* **50**, 127–131 (2014). <https://doi.org/10.1134/S1061830914020065>
18. Farnam, Y., Bentz, D., Hampton, A., Weiss, W.J.: Acoustic emission and low-temperature calorimetry study of freeze and thaw behavior in cementitious materials exposed to sodium chloride salt. *Transp. Res. Rec.* **2441**, 81–90 (2014). <https://doi.org/10.3141/2441-11>
19. Farnam, Y., Bentz, D., Sakulich, A., Flynn, D., Weiss, J.: Measuring freeze and thaw damage in mortars containing deicing salt using a low-temperature longitudinal guarded comparative calorimeter and acoustic emission. *Adv. Civ. Eng. Mater.* **3**, 20130095 (2014). <https://doi.org/10.1520/acem20130095>
20. Húlan, T., Knappek, M., Minárik, P., Csáki, Š., Kaljuvee, T., Uibu, M.: Assessing the frost resistance of illite-based ceramics through the resonant frequency of free vibration and internal damping. In: Medved', I., Avsec, J., and Trník, A. (eds.) *AIP Conference Proceedings*. p. 040015. American Institute of Physics Inc., 22nd International Meeting of Thermophysics 2017, THERMOPHYSICS 2017 and 4th Meeting of the Conference Energy and Responsibility, EnRe 2017; Terchova; Slovakia; 12 September 2017 through 14 September 2017 (2017)
21. Húlan, T., Trník, A., Štubňa, I., Bačík, P., Kaljuvee, T., Vozár, L.: Development of Young's modulus of illitic clay during heating up to 1100 °C. *Mater. Sci.* **21**, 429–434 (2015). <https://doi.org/10.5755/j01.ms.21.3.7152>
22. Csáki, Š., Ondruška, J., Trnovcová, V., Štubňa, I., Dobroň, P., Vozár, L.: Temperature dependence of the AC conductivity of illitic clay. *Appl. Clay Sci.* **157**, 19–23 (2018). <https://doi.org/10.1016/j.clay.2018.02.026>
23. Sedmale, G., Randers, M., Rundans, M., Seglins, V.: Application of differently treated illite and illite clay samples for the development of ceramics. *Appl. Clay Sci.* **146**, 397–403 (2017). <https://doi.org/10.1016/j.clay.2017.06.016>
24. Wang, G., Zhang, H., Zhang, N.: In situ high temperature X-ray diffraction study of illite. *Appl. Clay Sci.* **146**, 254–263 (2017). <https://doi.org/10.1016/j.clay.2017.06.006>
25. Húlan, T., Knappek, M., Štubňa, I., Trník, A.: The microcracking in illite-based ceramics followed by acoustic emission. In: *Noise and Vibration in Practice: Peer-Reviewed Scientific Proceedings*. pp. 71–76. STU, Bratislava (2016)
26. Monteiro, S.N., Vieira, C.M.F.: The role of particle shape on the sintering of clay based ceramics. *Mater. Sci. Forum.* **660–661**,

- 88–93 (2010). <https://doi.org/10.4028/www.scientific.net/MSF.660-661.88>
27. Heimann, R.B.: *Classic and Advanced Ceramics: From Fundamentals to Applications*. Wiley, Weinheim (2010)
28. Landry, M.R.: Thermoporometry by differential scanning calorimetry: Experimental considerations and applications. *Thermochim. Acta.* **433**, 27–50 (2005). <https://doi.org/10.1016/j.tca.2005.02.015>

Publisher's Note Springer Nature remains neutral with regard to jurisdictional claims in published maps and institutional affiliations.